Elastic and inelastic scattering for the ^{10}B + ^{58}Ni system at near-barrier energies

V. Scarduelli,[1] E. Crema,[1] V. Guimarães,[1] D. Abriola,[2] A. Arazi,[2,3] E. de Barbará,[2] O. A. Capurro,[2] M. A. Cardona,[2,3]
J. Gallardo,[2,3] D. Hojman,[2,3] G. V. Martí,[2] A. J. Pacheco,[2,3] D. Rodrígues,[2,3] Y. Y. Yang,[4] N. N. Deshmukh,[1] B. Paes,[5]
J. Lubian,[5] D. R. Mendes Junior,[5] V. Morcelle,[6] and D. S. Monteiro[7,8]

[1]*Instituto de Física, Universidade de São Paulo, Rua do Matão 1371, 05508-090 São Paulo, São Paulo, Brazil*
[2]*Laboratorio TANDAR, Comisión Nacional de Energía Atómica, Avenida General Paz 1499, B1650KNA San Martín, Buenos Aires, Argentina*
[3]*Consejo Nacional de Investigaciones Científica y Técnicas, Avenida Rivadavia 1917, C1033AAJ Buenos Aires, Argentina*
[4]*Institute of Modern Physics, Chinese Academy of Sciences, Lanzhou 730000, China*
[5]*Instituto de Física, Universidade Federal Fluminense, Avenida Litoranea s/n, Gragoatá, 24210-340 Niterói, Rio de Janeiro, Brazil*
[6]*Departament of Physics, Universidade Federal Rural do Rio de Janeiro, 23890-000 Seropédica, Rio de Janeiro, Brazil*
[7]*Universidade Federal da Integração Latino-Americana, Instituto Latino-Americano de Ciências da Vida e da Natureza,*
Foz do Iguaçu, Paraná, Brazil
[8]*Department of Physics, University of Notre Dame, South Bend, Indiana 46556, USA*

Full angular distributions of the ^{10}B elastically and inelastically scattered by ^{58}Ni have been measured at different energies around the Coulomb barrier. The elastic and inelastic scattering of ^{10}B on a medium mass target has been measured for the first time. The obtained angular distributions have been analyzed in terms of large-scale coupled reaction channel calculations, where several inelastic transitions of the projectile and the target, as well as the most relevant one- and two-step transfer reactions have been included in the coupling matrix. The roles of the spin reorientation, the spin-orbit interaction, and the large ground-state deformation of the ^{10}B, in the reaction mechanism, were also investigated. The real part of the interaction potential between projectile and target was represented by a parameter-free double-folding potential, whereas no imaginary potential at the surface was considered. In this sense, the theoretical calculations were parameter free and their results were compared to experimental data to investigate the relative importance of the different reaction channels. A striking influence of the ground-state spin reorientation of the ^{10}B nucleus was found, while all transfer reactions investigated had a minimum contribution to the dynamics of the system. Finally, the large static deformation of the ^{10}B and the spin-orbit coupling can also play an important role in the system studied.

I. INTRODUCTION

Elastic and inelastic scatterings between nuclei have been employed to investigate both nuclear structure and reaction mechanisms since Rutherford's experiments. As is well known, when one or both colliding nuclei have nonzero spin and ground-state static deformation, the interaction potential describing the system is much more complex than a simple spherical optical potential. This is because quadrupole terms, spin-orbit potential and other spin-dependent terms should be explicitly considered in the total effective potential. In the past, the relative influence of these terms in the total potential was largely investigated. Six decades ago, Blair [1] first suggested that elastic scattering of heavy nuclei could be affected by its ground-state quadrupole moments. In the 1970s, a large number of important studies were dedicated to the understanding of the influence of nuclear spin and nuclear ground-state deformation on the elastic angular distribution. For instance, Satchler [2,3] put in evidence that the observed differences between elastic-scattered light particles by even- and odd-mass heavy targets, at energies well above the Coulomb barrier, were mainly due to quadrupole scattering allowed for the odd target. However, Parks *et al.* [4] showed that, even with a more massive projectile and a lighter target, a strong quadrupole effect was responsible for the differences in the elastic scattering of ^{10}B, ^{11}B, and ^{12}C by ^{27}Al at large angles

and high bombarding energies. In this work, the oscillatory behavior at backward angles of the angular distributions for the ^{10}B projectile was damped due to its larger quadrupole moment. This damping effect was found to be less important for the ^{11}B and did not exist at all for the ^{12}C projectile. To investigate the oscillatory behavior and to show more clearly the damping effect in the angular distributions provoked by the quadrupole moments, the same authors measured the elastic-scattering angular distributions for the lighter systems ^{10,11}B + ^{16}O, at energies well above the Coulomb barrier [5]. Again, the oscillations in the elastic angular distributions for the ^{10}B + ^{16}O system were much more damped compared to the ones for the ^{11}B + ^{16}O system. And again, the explanation given by the authors was also the large quadrupole moment of the ^{10}B compared to the one for the ^{11}B isotope. In addition, despite the oscillation damping, it is important to observe that a large quadrupole moment can produce also an increase in the average elastic differential cross sections at larger angles. Another important conclusion of the later cited work is the necessity of coupled-channel calculations to take into account the influence of ground-state deformation on the reaction mechanism. More recently, several other works had been dedicated to investigate these issues. For instance, by bombarding odd-mass nuclei targets with medium-mass projectiles the same results discussed above were observed; i.e., the nucleus static deformation has an important effect on

the reaction mechanism at energies well above the Coulomb barrier [6,7].

As mentioned above, another phenomenon largely investigated in the past was the spin-orbit coupling effect in the collisions between nuclei [8–13]. In particular, due to the $(d + \alpha)$- and $(t + \alpha)$-cluster structures of the ^{6,7}Li isotopes, they were largely employed in both experiments and theoretical calculations to investigate the importance of spin-orbit interaction potential. Those works revealed an appreciable effect of the spin-orbit couplings on the elastic and inelastic processes at high bombarding energies. However, when heavier projectiles are involved, the spin-orbit contribution to the effective interaction potential is very low, even at high energies. Owing to the larger grazing angular momenta for heavier projectiles, the centrifugal potential increases more rapidly and dominates the process, despite the large $\langle \vec{L} \cdot \vec{S} \rangle$ expectation value. Therefore, a good experimental condition to investigate the spin-orbit interaction is to use a light high-spin projectile, at not very high bombarding energy. In this sense, the ^{10}B nucleus has $J^{\pi} = 3^+$ and a very large ground-state deformation, being a very good candidate. The $\langle \vec{L} \cdot \vec{S} \rangle$ expectation value for ^{10}B will be much larger than, for instance, the ^{6,7}Li projectiles. However, when nuclei with ground-state deformation are involved, another phenomenon can play an important role in the reaction mechanism: the ground-state reorientation. We have already investigated this process for the ^{16}O + ^{63}Cu system at energies nearly below and above the Coulomb barrier [14]. The target ^{63}Cu is a medium-mass odd nucleus with a large oblate deformation ($Q = -21.1$ fm^2). It has been found that its ground-state quadrupole momentum reorientation has a very important influence on the reaction mechanism. Recently, we also investigated the existence of this phenomenon for the light ^{11}B projectile bombarding the spherical target ^{58}Ni at energies below and above the Coulomb barrier [15]. In this work, an important influence of the ground-state reorientation of the ^{11}B in the reaction mechanism was observed, with almost no contribution from transfer reactions. By using large-scale coupled reaction channel calculations, without any imaginary potential at the interaction surface, the relative importance of the different reaction channels in the reaction mechanism can be investigated. It should be emphasized that our analysis is very different from the older ones cited above since our interest was not in finding optical potentials which would fit experimental angular distributions.

In the present work, we report on the measurements of elastic and inelastic scatterings for the ^{10}B + ^{50}Ni system, at energies below and above the Coulomb barrier. The aim of this study is to take advantage of the large spin and static deformation of the ^{10}B nucleus ($J^{\pi} = 3^+$ and $Q = +8.47$ fm^2) to investigate the reaction processes discussed above. The new data for the elastic and inelastic angular distributions are compared to complete coupled-channel calculations, where a large amount of inelastic and transfer channels were included in the coupling matrix, as well as the reorientation and spin-orbit channels.

The paper is organized as follows. Section II contains a description of the experiment. Section III presents the data and gives the results of the coupled-channel calculations. Section IV is dedicated to the coupled reaction channel calculations, and Sec. V is devoted to investigation of the influence of the projectile deformation and the spin-orbit coupling on the reaction mechanism of the system studied. Finally, the last section presents a summary of this work.

II. EXPERIMENTAL SETUP AND MEASUREMENTS

Angular distributions of the ^{10}B + ^{58}Ni elastic and inelastic scattering were measured using the ^{10}B stable beam from the 20 UD tandem accelerator at the TANDAR laboratory (Buenos Aires, Argentina) at energies below and above the Coulomb barrier, namely, $E_{\text{lab}} = 19.0, 21.0, 23.0, 24.0, 25.0$, and 35.0 MeV. The nominal Coulomb barrier for this system in the laboratory frame is around 23 MeV. The beam intensity ranged from 3 to 10 pnA. The ^{58}Ni targets, enriched at 99.84%, had thicknesses of 100 and 144 μg/cm^2 with a very thin layer of ^{197}Au (12 and 20 μg/cm^2, respectively). The energies considered in the analysis were those at the half-target thickness, which, for these thin targets, a correction of about 100 keV was required.

The setup for this measurement consisted of an array of eight planar silicon surface-barrier detectors, 300μm thick, with an angular separation of 5° between adjacent detectors. More details about this setup and the data-acquisition system are given in Ref. [16]. In addition to the array, two monitors, silicon detectors, were placed at forward angles ($\theta_{\text{lab}} \pm 16.0°$) from the beam direction for absolute normalization purpose. To confirm the calibration and obtain, with good accuracy, the solid angle for each detector, we measured in subsequent runs the elastic scattering of ^{10}B on a gold target 150 μg/cm^2 thick. The obtained solid angles subtended by the array of eight detectors were 0.285, 0.123, 0.193, 0.285, 0.296, 0.383, 0.561 and 0.696 msr, respectively.

The angular distributions were measured from $\theta_{\text{lab}} = 27.0°$ to 172.2°, at lower energies, and from $\theta_{\text{lab}} = 27.0°$ to 125.2° for higher energies. The statistical uncertainties in the cross sections ranged from 0.3% to 8% starting from the most forward to the most backward angles, for the lower energies, and 0.2% to 27% for the highest energy of $E_{\text{lab}} = 35.0$ MeV. A very small contribution from carbon, oxygen, and silicon contaminants in the target were observed and correctly taken into account. Contributions from the inelastic-scattering channels were determined for the first 2^+ excited state of the ^{58}Ni nucleus ($E^* = 1.454$ MeV) and first excited state 1^+ of the ^{10}B nucleus ($E^* = 0.718$ MeV), and angular distributions were obtained. An energy spectrum showing these inelastic contributions, measured at $E_{\text{lab}} = 35$ MeV and at $\theta_{\text{lab}} = 57.5°$, is presented in Fig. 1, which shows that the energy resolution is good enough to resolve the different inelastic events. The measured elastic angular distributions are shown in Fig. 2, where we can observe, as the bombarding energy increases, more reaction channels are being opened and the elastic cross section deviates from the Rutherford cross section. To reveal which channels are responsible for the deviation is the aim of the next sections. The lines in Fig. 2 are the coupled-channel calculations discussed below. The measured inelastic angular distributions are presented in Figs. 4 and 5 compared to the theoretical results of the same calculations.
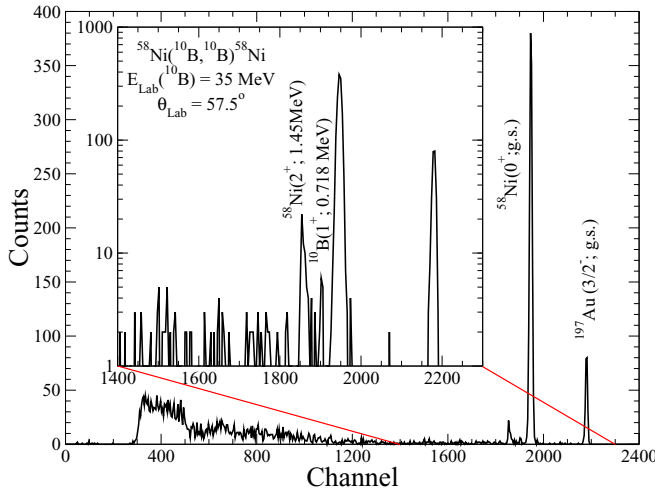
FIG. 1. A typical energy spectrum for the ^{10}B + ^{58}Ni system measured at $\theta_{lab} = 57.5°$ and $E_{lab} = 35$ MeV. The contributions of the excited states ^{58}Ni (2^+,1.45 MeV) and ^{10}B (1^+,0.718) are indicated.

III. COUPLED-CHANNEL CALCULATIONS

The first step of our theoretical analysis was to calculate the angular distributions based on the coupled-channel (CC) method. This can be considered a quite physically satisfying approach since we can take into account the nonelastic channels, especially the one arising from collective excitation, into the elastic scattering. We adopted the parameter-free double-folding São Paulo potential (SPP) [17] as the real bare potential to simulate the nuclear interaction between projectile and target nuclei. It has already been demonstrated that the SPP can be considered a reliable starting point for CC calculation even for systems with unstable nuclei [18]. For the energy range considered in the present investigation (near the Coulomb barrier), the SPP is almost energy independent and the relevant feature for the calculations is its double-folding
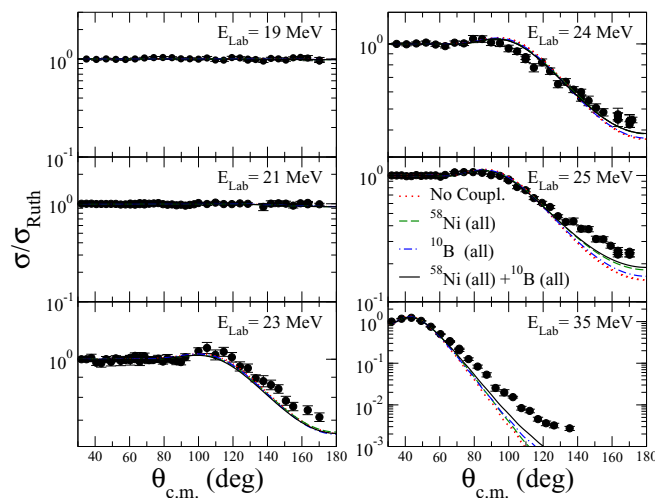
characteristic. No imaginary surface potential was employed in our coupled-channel calculation because all relevant reaction channels were explicitly taken into account. We also considered a short-range imaginary potential to simulate the absorption of flux due to fusion. This short-range potential had a Woods-Saxon shape with the parameters $V_i = 80$ MeV, $r_i = 0.9$ fm, and $a_i = 0.5$ fm. This set of parameters was used in several previous works [14,15,19], and the final results are not very sensitive to this particular choice. All the calculations were performed using the code FRESCO [20].

A. Couplings effects on the elastic-scattering angular distribution

In this section, we present the comparison between the theoretical calculations and data for the elastic angular distributions of the ^{10}B + ^{58}Ni system. The spin, parity, and energy of the excited states investigated in the calculation for both ^{10}B projectile and ^{58}Ni target are listed in Table I. The $B(E2)$ and $B(E3)$ experimental values available in the literature [21] for the transitions included in the calculations are listed in Table II. To investigate the effect of each inelastic channel, and the interference between them on the reaction dynamic of this system, we added one by one the inelastic channels of

TABLE I. Spin-parity and energy of the states in ^{58}Ni and ^{10}B, from the NNDC database [21], considered in the coupled-channel calculations.

J^π ^{58}Ni	E (MeV)	J^π ^{10}B	E (MeV)
0^+	g.s.	3^+	g.s.
2^+	1.4542	1^+	0.718
4^+	2.4592	1^-	2.154
2^+	2.7754	3^+	4.774
0^+	2.9425	2^+	8.895
2^+	3.0378		
2^+	3.2636		

TABLE II. All inelastic transitions for ^{58}Ni and ^{10}B used in the coupled-channel calculations.

E (keV)	E_γ (keV)	$J_F \rightleftarrows J_i$	$B(E2)$ (W.u.)	$\langle J_f|E2|J_i\rangle$ (e^2 fm^4)	δ_2 (fm)
			^{58}Ni		
1454.28	1454.28	$0^+ \rightleftarrows 2^+$	10	25.8224	0.9415
2459.21	1004.8	$2^+ \rightleftarrows 4^+$	11.2	36.6642	1.3368
2775.42	2775.42	$0^+ \rightleftarrows 2^+$	0.029	1.3906	0.0507
2942.56	167.2	$2^+ \rightleftarrows 0^+$	21	16.7348	0.6102
2942.56	1488.3	$2^+ \rightleftarrows 0^+$	0.0004	0.0730	0.0027
3037.86	3037.7	$0^+ \rightleftarrows 2^+$	1.15	8.7568	0.3193
3263.66	3263.4	$0^+ \rightleftarrows 2^+$	1.9	11.2557	0.4104
			^{10}B		
718.38	718.353	$3^+ \rightleftarrows 1^+$	3.24	3.5269	1.2938
2154.27	2154.1	$3^+ \rightleftarrows 1^+$	1.33	2.2597	0.8289
4774	4054.8	$1^+ \rightleftarrows 3^+$	15.4	11.7454	4.3087
8895	8890	$3^+ \rightleftarrows 2^+$	8.5	7.3749	2.7054

FIG. 2. Elastic scattering angular distribution for the ^{10}B + ^{58}Ni system at $E_{lab} = 19.0, 21.0, 23.0, 24.0, 25.0,$ and 35.0 MeV. The lines are results of coupled-channel calculations as indicated.
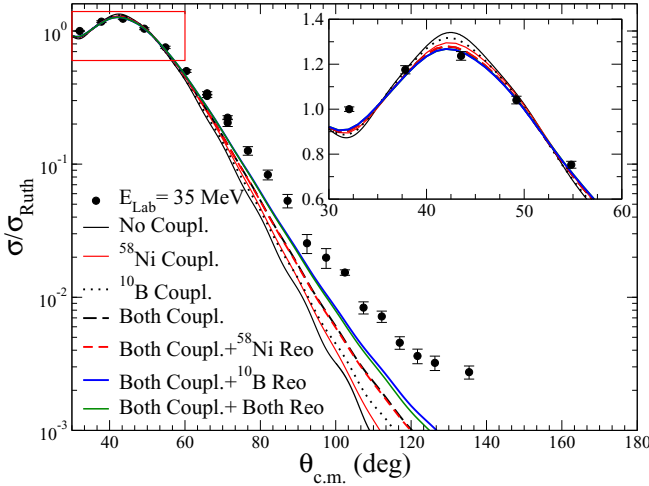
FIG. 3. Elastic scattering angular distribution for the ^{10}B + ^{58}Ni system at $E_{\rm lab} = 35.0$ MeV. The lines are results of coupled-channel calculations as indicated.

the projectile and target states in the coupling scheme. The comparison of this theoretical procedure to the data, for all measured elastic angular distributions, is displayed in Fig. 2. In this figure the dotted line is the prediction of the CC calculation when all the reaction channels are closed (no couplings), the dashed green line represents the results when coupling all states of the target are included, the dashed-dotted blue line corresponds to the calculation where only the excited states of the projectile are included, and the solid line represents the cumulative results when excited states of both target and projectile are included in the coupling matrix. As can be observed in Fig. 2, the effect of the couplings is very small for the energies below the Coulomb barrier ($E_{\rm lab} = 19.0$ and 21.0 MeV), and the calculation with no couplings describes well the experimental elastic cross sections. However, for energies at the barrier and above ($E_{\rm lab} = 23.0, 24.0, 25.0,$ and 35.0 MeV) the situation is completely different. As the bombarding energy increases, reaction channels are being progressively opened, and the coupling of these channels becomes necessary to understand the dynamics of the reaction.

To follow the dynamics of the reaction in more detail, the angular distribution measured at $E_{\rm lab} = 35.0$ is shown separately in Fig. 3, where the forward angle region (rainbow peak) is presented in linear scale in the inset of the figure, where the intention was to reveal the competition between channels at forward angles. This figure shows that the inelastic channels increase the elastic cross sections at backward angles, while the inset shows they reduce the elastic cross sections at forward angles. It means that the effect of these reaction channels is to deviate the elastic flux from forward to backward angles. Despite the figures present the global results for projectile and target, the most relevant inelastic channels are the quadrupole vibrations: ^{10}B (1$^+$, $E^* = 0.718$ MeV) and ^{58}Ni (2$^+$, $E^* = 1.454$ MeV), respectively. A very interesting result is revealed in these calculations: the couplings of the projectile excited states (dotted black line) have a stronger influence on the reaction mechanism than the target ones (solid

red line). This is in opposite direction of what was observed for the ^{11}B + ^{58}Ni system [15]. However, this result comes in the same direction as Parks's work [4], where the ^{10}B has also a stronger influence on the reaction mechanism due to its larger deformation compared to that of the ^{11}B.

Despite the inclusion of almost all excited states of the projectile and target in the calculation (for which there are available $B(E2)$ and $B(E3)$ experimental data), our coupled-channel calculations did not agree with the measured elastic cross sections. To improve the agreement, we included the reorientation channels for the ground state of the projectile and for excited states of the target in the coupling matrix. The solid blue line in Fig. 3 shows the striking effect of the ground-state reorientation of the ^{10}B on the reaction dynamics, as compared to the other inelastic channels. The results of these calculations reveal also that the spin reorientation of the excited states of the target (dotted red line) has a minor influence in this system. These results were recently observed with lighter targets [22,23], as well as for the ^{11}B + ^{58}Ni system also studied by our group [15].

Finally, we would like to emphasize once more that these calculations are parameter free and no artificial superficial imaginary potential has been used. In this approach, the absorption from the elastic channel is produced by the real process of opening inelastic channels.

B. Inelastic-scattering angular distributions

Angular distributions for the inelastic scattering of the target and projectile first-excited states have also been measured. Six angular distributions for the inelastic scattering of the target first-excited state, ^{58}Ni (2$^+$,1.454 MeV) have been measured at $E_{\rm lab} = 19.0, 21.0, 23.0, 24.0, 25.0,$ and 35.0 MeV, and three angular distributions for the inelastic scattering of the projectile first-excited state ^{10}B (1$^+$,0.718 MeV) have been measured at $E_{\rm lab} = 24.0, 25.0,$ and 35.0 MeV. These angular distributions are shown in Figs. 4 and 5, where the lines are the results of the calculations described in the previous section.

As can be seen in the figures, the present parameter-free coupled-channel calculation agrees very well with data for all measured energies. Even the small oscillations in all angular distributions were predicted by our theoretical approach. These results can be considered an important confirmation of the self-consistency of our coupled-channel calculations.

IV. COUPLED REACTION CHANNEL CALCULATIONS

In this section we study the effect of some transfer channels on the elastic scattering of the ^{10}B + ^{58}Ni system. The transfer reactions considered here were the one-neutron stripping (^{58}Ni(^{10}B,^{9}B)^{59}Ni), the one-neutron pickup (^{58}Ni(^{10}B,^{11}B)^{57}Ni), the one-proton pickup (^{58}Ni(^{10}B, ^{11}C) ^{57}Co), and the one-deuteron pickup (^{58}Ni(^{10}B,^{12}C)^{56}Co), which are the channels with lower-mass transfer and positive or not too negative Q values.

For this purpose, exact finite range coupled reaction channel (CRC) calculations were performed. The double-folding SPP [17] was used for the real-part optical potential of the entrance partition, and a Woods-Saxon for the imaginary part, depth,
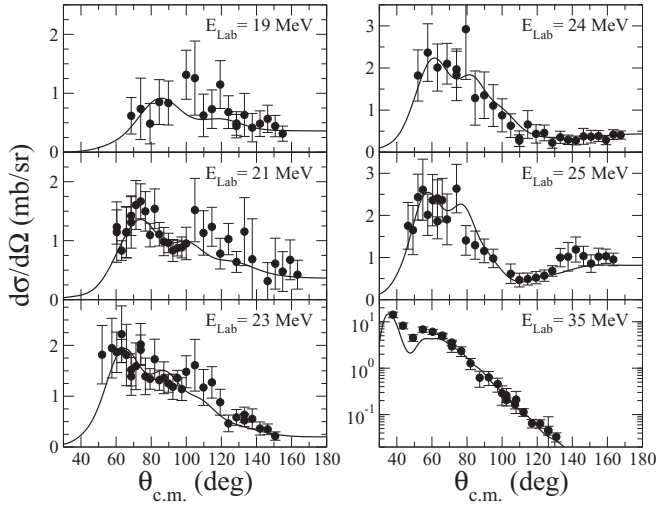
FIG. 4. Inelastic scattering angular distributions for the ^{10}B + ^{58}Ni (2^+,1.454) first excited state measured at $E_{lab} = 19.0, 21.0, 23.0,$ 24.0, 25.0, and 35.0 MeV. The solid lines are the results of the CC calculations.

FIG. 6. Coupling scheme of the projectile and target overlaps used in the one-neutron pickup transfer reaction.

radius, and diffuseness given by $V = 80$ MeV, $r_i = 0.9$ fm, and $a_i = 0.5$ fm. This was exactly the same optical potential used in the previous section for the coupled-channel calculations including only the inelastic excitation of the projectile and the target. In the outgoing partition, the imaginary part was assumed to have the same radial dependence of the real part, but multiplied by strength coefficient $N_I = 0.78$, because no couplings were explicitly considered. This strength coefficient was shown to be suitable for describing the elastic-scattering cross section for many systems [24] at energies above the Coulomb barrier, where no relevant couplings to the elastic channel are expected.

To generate the single-particle wave functions, Woods-Saxon form factors were used. The reduced radii and dif-
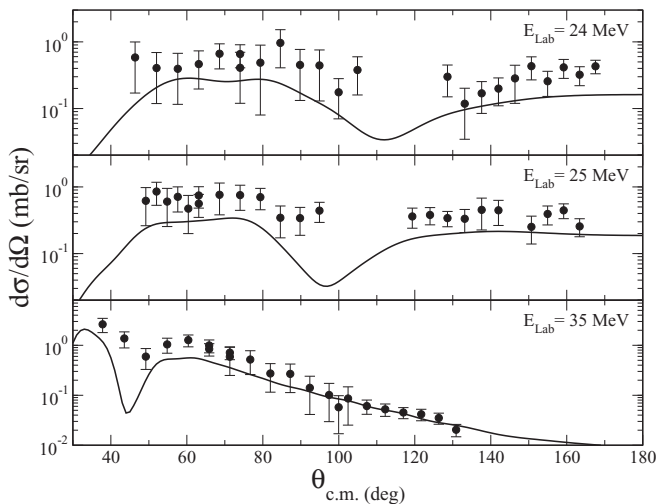

FIG. 5. Inelastic scattering angular distributions for the ^{10}B(1+,0.718)+^{58}Ni measured at $E_{lab} = 24.0, 25.0,$ and 35.0 MeV. The solid lines are the results of the CC calculations.
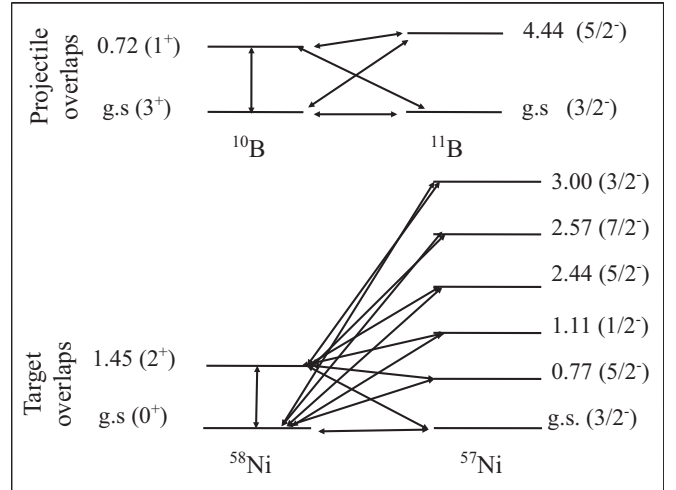
fuseness were set equal to 1.25 and 0.65 fm, respectively, for all the ^{9}B, ^{58}Ni, ^{10}B, ^{57}Co, ^{57}Ni, and ^{56}Co nuclei. The depths of the Woods-Saxon potentials were varied to reproduce the experimental binding energies for one neutron, one proton, or one deuteron.

The full complex remnant in coupling matrix elements, prior representation, and nonorthogonality corrections were adopted in the calculations. In the CRC calculations only the first excited state of the projectile and the target were included, to account for the more relevant inelastic couplings at the same time. The other states were not included to avoid very time consuming calculations.

First, we performed calculations including only the one-neutron pickup reaction to study its influence on the elastic scattering. Then all the transfer channels were included in one calculation.

For the ^{58}Ni(^{10}B,^{11}B)^{57}Ni reaction, full microscopic CRC calculations were performed. This can be done by performing shell model calculations for derivation of the spectroscopic amplitudes for the projectile and target overlaps. These spectroscopic amplitudes were derived using the NUSHELLX code [25]. To obtain the one-neutron spectroscopic information of the projectile overlaps, the p model space and effective interaction *ckpot* [26] was used. In this model space the ^{4}He nucleus is considered a closed core and the $1p_{1/2}$ and $1p_{3/2}$ orbitals are taken as valence space for both neutrons and protons. For the target overlaps, the fp model space and effective interaction *fpd6* [27] were used. In this model space the ^{40}Ca nucleus is considered a closed core and the $1f_{7/2}$, $1f_{5/2}$, $2p_{3/2}$, and $2p_{1/2}$ orbitals are taken as valence space for both neutrons and protons. The coupling scheme for one-neutron pickup is shown in Fig. 6. In Table III, the spectroscopic amplitudes used in the one-neutron pickup transfer reactions, concerning the projectile and target overlaps, are shown.

The results of CRC calculations for the one-neutron pickup reaction are shown in Fig. 7 by a dashed curve. The solid curve corresponds to the results of CC calculations shown in

TABLE III. Spectroscopic amplitudes used in the CRC calculations for one-neutron pickup transfer reactions, where j is the spin of the neutron orbitals.

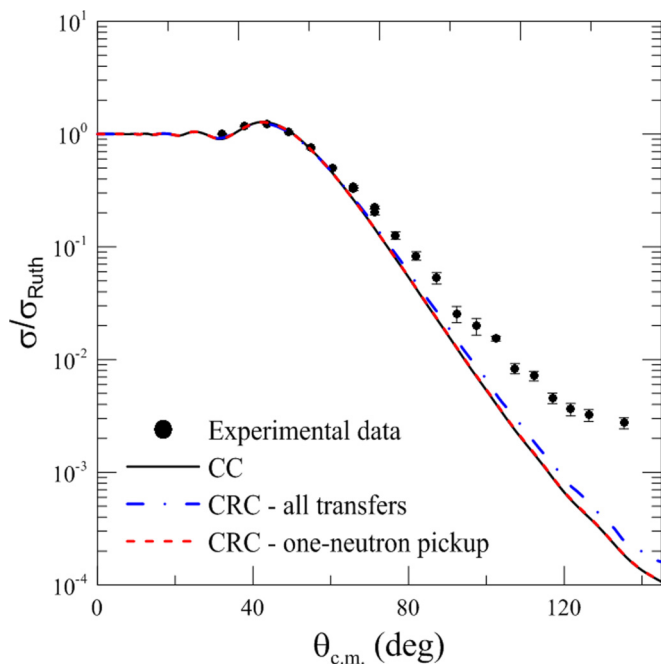| Initial state	Orbital	Final state	Spectroscopic amplitude
$^{10}B_{g.s.}(3_1^+)$	$(1p_{3/2})$	$^{11}B_{g.s.}(3/2^-)$	1.046
$^{10}B_{0.71}(1_1^+)$	$(1p_{1/2})$	$^{11}B_{g.s.}(3/2^-)$	0.437
	$(1p_{3/2})$		0.267
$^{10}B_{g.s.}(3_1^+)$	$(1p_{1/2})$	$^{11}B_{4.44}(5/2^-)$	−0.197
	$(1p_{3/2})$		0.310
$^{10}B_{0.71}(1_1^+)$	$(1p_{3/2})$	$^{11}B_{4.44}(5/2^-)$	−0.150
$^{58}Ni_{g.s.}(0^+)$	$(2p_{3/2})$	$^{57}Ni_{g.s.}(3/2_1^-)$	0.687
$^{58}Ni_{g.s.}(0^+)$	$(1f_{5/2})$	$^{57}Ni_{0.77}(5/2_1^-)$	−1.173
$^{58}Ni_{g.s.}(0^+)$	$(2p_{1/2})$	$^{57}Ni_{1.11}(1/2_1^-)$	−0.309
$^{58}Ni_{g.s.}(0^+)$	$(1f_{5/2})$	$^{57}Ni_{2.44}(5/2_2^-)$	0.079
$^{58}Ni_{g.s.}(0^+)$	$(1f_{7/2})$	$^{57}Ni_{2.57}(7/2_1^-)$	1.824
$^{58}Ni_{g.s.}(0^+)$	$(2p_{3/2})$	$^{57}Ni_{3.00}(3/2_2^-)$	0.022
	$(2p_{1/2})$		0.260
$^{58}Ni_{1.45}(2^+)$	$(2p_{3/2})$	$^{57}Ni_{g.s.}(3/2_1^-)$	0.483
	$(1f_{5/2})$		0.378
	$(2p_{1/2})$		−0.355
$^{58}Ni_{1.45}(2^+)$	$(2p_{3/2})$	$^{57}Ni_{0.77}(5/2_1^-)$	0.347
	$(1f_{5/2})$		−0.84
$^{58}Ni_{1.45}(2^+)$	$(2p_{3/2})$	$^{57}Ni_{1.11}(1/2_1^-)$	0.248
	$(1f_{5/2})$		−0.385
	$(2p_{1/2})$		0.009
$^{58}Ni_{1.45}(2^+)$	$(2p_{3/2})$	$^{57}Ni_{2.44}(5/2_2^-)$	−0.160
	$(1f_{5/2})$		−0.071
	$(2p_{3/2})$		0.141
$^{58}Ni_{1.45}(2^+)$	$(1f_{5/2})$	$^{57}Ni_{2.57}(7/2_1^-)$	0.001
	$(1f_{7/2})$		−0.233
	$(2p_{1/2})$		−0.002
$^{58}Ni_{1.45}(2^+)$	$(2p_{3/2})$	$^{57}Ni_{3.00}(3/2_2^-)$	−0.001
	$(1f_{5/2})$		0.063

FIG. 7. Comparison between the experimental data and the theoretical results for the elastic cross section.

reaction. The overlaps considered for the one-deuteron transfer reaction are shown in Fig. 8.

Concerning the one-deuteron and ^{6}Li stripping reactions, for the correspondent ejectiles ^{8}Be and ^{4}He, respectively, only the ground state was considered. For the residual nuclei ^{60}Cu and ^{64}Ga, a resonant state with parity 0^+ and energies 10.34 and 24.86 MeV, respectively, were considered in a such way as to represent the more important state according to the (E_{opt}) calculations. For the one-neutron stripping and one-proton pickup only the overlaps between the ground states were considered.

the previous section. From Fig. 7 one observes that the effect of this transfer channel on the elastic cross section is negligible.

Having in mind that the one-neutron pickup had no effect on the elastic channel, we studied the influence of the other transfer reactions (one-neutron stripping, one-proton and one-deuteron pickup, as well as one-deuteron and ^{6}Li stripping reactions) at the same time, using spectroscopic amplitudes equal to 1.0. Then, if some relevant effect was found, we would perform shell-model calculations to derive the spectroscopic factors for the corresponding overlaps. In the case of the transfer of charged particles (one proton and deuteron, stripping and pickup transfers) the optimal Q value and energy (E_{opt}) populated were determined, using the prescription proposed by Brink [28]. The E_{opt} found for the proton and deuteron transfer was −4.17 MeV, for the deuteron pickup and stripping was 3.16 MeV, and for the ^{6}Li stripping was 24.86 MeV. For this reason, we included target overlaps between ground state (g.s.) and the 2^+ state of ^{58}Ni and states up to 3.53 MeV of ^{56}Co for the deuteron pickup transfer
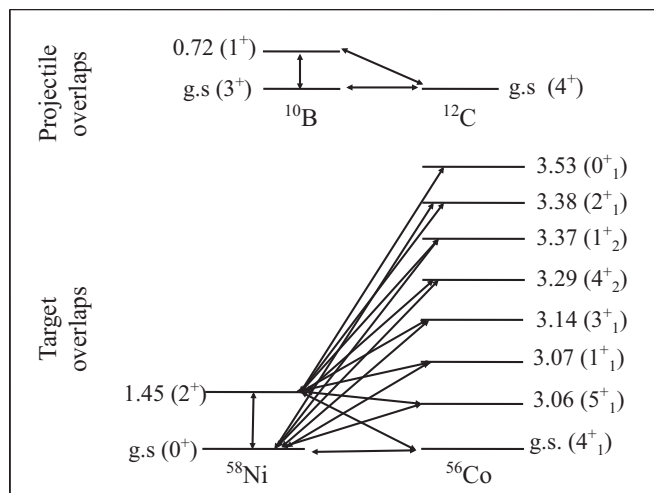

FIG. 8. Coupling scheme of the projectile and target overlaps used in the one-deuteron pickup reaction.

In Fig. 7 the result of CRC calculations including all the transfer channels is shown by the dot-dashed curve. From Fig. 7, one observes that the effect of these transfer reactions on the elastic cross section is small at the most backward angles and that the coupling to transfer channels is not enough to describe the experimental data. Even for the transfer reactions with large Q value such as those with ^{8}Be and ^{4}He as ejectiles, the influence in the elastic is negligible. For this reason, we did not perform detailed structure calculations for deriving microscopic spectroscopic amplitudes for the other channels for which the value 1.0 was adopted.

V. ^{10}B DEFORMATION AND SPIN-ORBIT INTERACTION

After the results of the previous large-scale calculations did not reproduce perfectly the experimental elastic data, we investigated other phenomena that could improve the agreement between the theoretical calculations and data. Breakup processes could be invoked to accomplish this role. However, all possible breakup channels of the ^{10}B nucleus have Q values that are largely negative and, in principle, do not have an important influence on the reaction mechanism. Another possible alternative is the use of a more realistic interaction potential. In all the previous calculations, the standard SPP was used to describe the real part of the interaction between projectile and target. The double-folding procedure of its theoretical approach employs average values of the charge and mass distribution parameters. It is well known that these average values were calculated over many experimental charge distributions and successfully describe the interaction of hundreds of systems. Nevertheless, as the ^{10}B deformation is very large, the average parameters of the standard SPP could not be adequate to describe our system. So, as an attempt, we construct the double-folding potential between projectile and target by considering explicitly the experimental charge distribution of the ^{10}B available in the literature [29]. Its mass distribution was assumed to be double the charge one. The result of the coupled-channel calculation (CCC) with this realistic double-folding potential, at $E_{\text{lab}} = 35.0$ MeV, is shown by the dashed green line in Fig. 9, where the dotted black line is the complete CCC result of Sec. III. The backward angle region is well described by the calculation. However, the inset in the figure shows that, in the forward angle region (Coulomb rainbow peak), the agreement is worst: the entire angular distribution is shifted by approximately 2.5°. In addition, the agreements of this calculation with the inelastic angular distributions also become worse.

Finally, we investigated the effect of spin-orbit coupling in the reaction dynamics of the system studied in this work. As mentioned in Sec. I, many systems with the ^{10}B nucleus present strong coupling of the large ^{10}B spin with the orbital movement. The radial form of the spin-orbit potential used here was the conventional derivative of a Woods-Saxon function. For this evaluation, the average radius and diffuseness of the Woods-Saxon function were kept constant, i.e., $r_0 = 1.06$ fm and $a_0 = 0.6$ fm, respectively. Then we varied the depth, V_0, of this spin-orbit potential to get the best agreement with data. The striking result of this procedure is shown by the solid blue line in Fig. 9 for the bombarding energy of $E_{\text{lab}} = 35.0$ MeV.
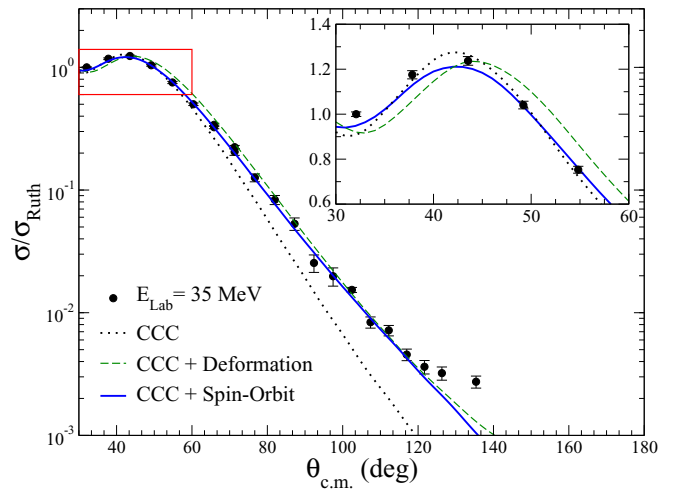

FIG. 9. Elastic scattering angular distributions for the ^{10}B + ^{58}Ni system measured at $E_{\text{lab}} = 35.0$ MeV. The lines are discussed in the text.

An excellent agreement was achieved, in almost the entire angular region, when the potential depth was $V_0 = 3.0$ MeV, as shown by the solid blue line in the figure. In addition, its inset reveals that, different from the previous calculation, the spin-orbit interaction gives a very good description of the main Fresnel peak. In addition, in the opposite direction of the previous calculation with the realistic bare potential, the inelastic angular distributions were affected very little by the inclusion of the spin-orbit potential. To show the sensitivity of this result with the depth of the Woods-Saxon potential, Fig. 10 presents the results of the calculations for $V_0 = 1.0$, 2.0, 3.0, and 4.0 MeV. The inset in this figure shows the χ^2/N of the fits to experimental data as a function of the V_0 values employed. As can be seen by the curves themselves and by
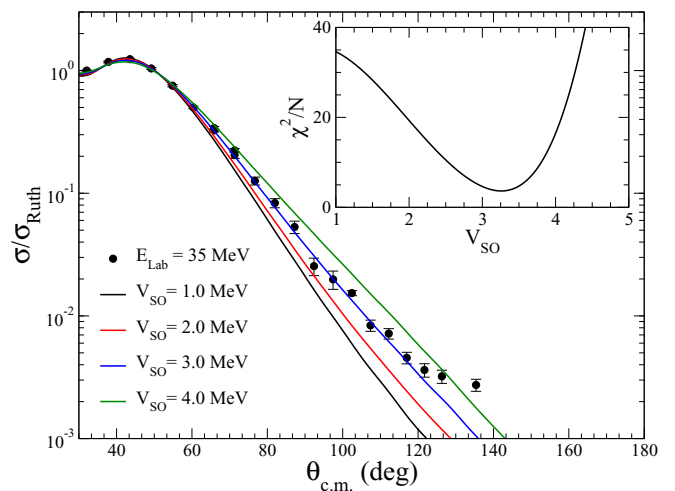

FIG. 10. Elastic scattering angular distributions for the ^{10}B + ^{58}Ni system measured at $E_{\text{lab}} = 35.0$ MeV. The lines correspond to CC calculations with spin-orbit interaction for $V_0 = 1.0$, 2.0, 3.0, and 4.0 MeV. The inset shows the χ^2/N of the fits to experimental data as a function of the V_0 values employed.

the χ^2/N function, the calculation is very sensitive to the Woods-Saxon potential. Furthermore, it is worth emphasizing that our spin-orbit potential is very similar to the ones used in the literature for ^{6,7}Li and ^{10,11}B projectiles, as for instance in Refs. [9,10,12]. So, in conclusion, there is a strong evidence that the spin-orbit coupling could play an important role in the reaction mechanism of the ^{10}B + ^{58}Ni system at the bombarding energy region investigated.

VI. SUMMARY AND CONCLUSIONS

Full angular distributions for elastic and inelastic scattering of ^{10}B on ^{58}Ni have been measured at different bombarding energies around the Coulomb barrier. Elastic scattering of ^{10}B has been measured for the first time on a medium-mass target. We also measured six inelastic scattering angular distributions from the first excited state of the ^{58}Ni target, and three for the first excited state of the ^{10}B projectile. The obtained angular distributions have been analyzed in terms of a large-scale coupled reaction channel calculation, where several inelastic transitions of the projectile and the target, as well as the most relevant one- and two-step transfer reactions, were included in the coupling matrix. Moreover, the roles of the spin reorientation, the spin-orbit interaction, and the large ground-state deformation of ^{10}B in the reaction mechanism were also investigated. The real part of the interaction potential between projectile and target was represented by a parameter-free double-folding potential, and no imaginary potential at the surface was considered. In this sense, the theoretical calculations were parameter free and their results were compared to experimental data to investigate the relative importance of the different reaction channels. All inelastic angular distributions were well described by the coupled-channel calculations. A striking influence on the reaction mechanism of the ground-state spin reorientation of the ^{10}B nuclei was found, while all transfer reactions investigated had a small contribution to the dynamics of the system. Finally, the large static deformation of ^{10}B and the spin-orbit coupling can also play a strong role in the system studied. An important fact that reinforces this conclusion is the similarity of our spin-orbit potential with others from the literature used to explain systems involving the ^{6,7}Li and ^{10,11}B nuclei [9,10,12].

[1] J. S. Blair, Phys. Rev. **115**, 928 (1959).

[2] G. R. Satchler, Nucl. Phys. A **45**, 197 (1963).

[3] G. R. Satchler and C. B. Fulmer, Phys. Lett. B **50**, 309 (1974).

[4] L. A. Parks, K. W. Kemper, A. H. Lumpkin, R. I. Cutler, L. H. Harwood, D. Stanley, P. Nagel, and F. Petrovich, Phys. Lett. B **70**, 27 (1977).

[5] L. A. Parks, D. P. Stanley, L. H. Courtney, and K. W. Kemper, Phys. Rev. C **21**, 217 (1980).

[6] V. Hnizdo, K. W. Kemper, and J. Szymakowski, Phys. Rev. Lett. **46**, 590 (1981).

[7] A. T. Rudchik *et al.*, Nucl. Phys. A **662**, 44 (2000).

[8] H. Amakawa and K.-I. Kubo, Nucl. Phys. A **266**, 521 (1976).

[9] S. Ohkubo, Phys. Rev. C **25**, 2498 (1982).

[10] F. Petrovich, D. Stanley, L. A. Parks, and P. Nagel, Phys. Rev. C **17**, 1642 (1978).

[11] M. B. Golin and S. Kubono, Phys. Rev. C **20**, 1347 (1979).

[12] H. Nishioka, R. C. Johnson, J. A. Tostevin, and K.-I. Kubo, Phys. Rev. Lett. **48**, 1795 (1982).

[13] K. Rusek *et al.*, Nucl. Phys. A **407**, 208 (1983).

[14] J. M. B. Shorto, E. Crema, R. F. Simões, D. S. Monteiro, J. F. P. Huiza, N. Added, and P. R. S. Gomes, Phys. Rev. C **78**, 064610 (2008).

[15] N. N. Deshmukh, V. Guimarães, E. Crema, D. Abriola, A. Arazi, E. de Barbará, O. A. Capurro, M. A. Cardona, J. Gallardo, D. Hojman, G. V. Martí, A. J. Pacheco, D. Rodrígues, Y. Y. Yang, A. N. Deshmukh, D. R. Mendes, Jr., V. Morcelle, V. Scarduelli, and D. S. Monteiro, Phys. Rev. C **92**, 054615 (2015).

[16] D. Abriola *et al.*, Nucl. Instrum. Methods Phys. Res., Sect. B **268**, 1793 (2010).

[17] L. C. Chamon, B. V. Carlson, L. R. Gasques, D. Pereira, C. De Conti, M. A. G. Alvarez, M. S. Hussein, M. A. Candido Ribeiro, E. S. Rossi, Jr., and C. P. Silva, Phys. Rev. C **66**, 014610 (2002).

[18] E. Crema, P. R. S. Gomes, and L. C. Chamon, Phys. Rev. C **75**, 037601 (2007).

[19] J. F. P. Huiza, E. Crema, D. S. Monteiro, J. M. B. Shorto, R. F. Simões, N. Added, and P. R. S. Gomes, Phys. Rev. C **75**, 064601 (2007).

[20] I. J. Thompson, Comput. Phys. Rep. **7**, 167 (1988).

[21] Evaluated Nuclear Structure Data Files, National Nuclear Data Center, Brookhaven National Laboratory, http://www.nndc.bnl.gov.

[22] A. T. Rudchik *et al.*, Nucl. Phys. A **941**, 167 (2015).

[23] S. Yu. Mezhevych *et al.*, Eur. Phys. J. A **50**, 4 (2014).

[24] L. R. Gasques, L. C. Chamon, P. R. S. Gomes, and J. Lubian, Nucl. Phys. A **764**, 135 (2006).

[25] W. D. M. Rae, http://www.garsington.eclipse.co.uk.

[26] S. Cohen and D. Kurath, Nucl. Phys. A **73**, 1 (1965).

[27] W. Richter, M. V. D. Merwe, R. Julies, and B. Brown, Nucl. Phys. A **523**, 325 (1991).

[28] D. M. Brink, *Semi-classical Methods for Nucleus-Nucleus Scattering* (Cambridge University Press, Cambridge, UK, 1985).

[29] H. De Vries, C. W. De Jager, and C. De Vries, At. Data Nucl. Data Tables **36**, 35 (1987).